

Article

Sucrose-Assisted Solution Combustion Synthesis of Doped Strontium Ferrate Perovskite-Type Electrocatalysts: Primary Role of the Secondary Fuel

Maria Laura Tummino ^{1,2}, Leonarda Francesca Liotta ², Giuliana Magnacca ^{1,3},
Massimiliano Lo Faro ⁴, Stefano Trocino ⁴, Sabrina Campagna Zignani ⁴,
Antonino Salvatore Aricò ⁴ and Francesca Deganello ^{2,*}

¹ Department of Chemistry, University of Turin, Via P. Giuria 7, 10125 Torino, Italy; marialaura.tummino@unito.it (M.L.T.); giuliana.magnacca@unito.it (G.M.)

² Institute for the Study of Nanostructured Materials (ISMN), (Italian) National Research Council (CNR), Via Ugo La Malfa 153, 90146 Palermo, Italy; leonardafrancesca.liotta@cnr.it

³ NIS and INSTM Reference Centre, Via P. Giuria 7, 10125 Torino, Italy

⁴ Institute for Advanced Energy Technologies “Nicola Giordano” (ITAE), (Italian) National Research Council (CNR), via Salita S. Lucia sopra Contesse 5, 98126 Messina, Italy; massimiliano.lofaro@cnr.it (M.L.F.); stefano.trocino@itae.cnr.it (S.T.); zignani@itae.cnr.it (S.C.Z.); arico@itae.cnr.it (A.S.A.)

* Correspondence: francesca.deganello@cnr.it; Tel.: +39-091-680-9387

Received: 20 December 2019; Accepted: 15 January 2020; Published: 18 January 2020



Abstract: The methodologies and experimental conditions used for the synthesis of cathode materials for electrochemical devices strongly influence their electrocatalytic performance. In particular, solution combustion synthesis is a convenient and versatile methodology allowing a fine-tuning of the properties of the material. In this work, we used for the first time a sucrose assisted-solution combustion synthesis for the preparation of Cerium and Cobalt-doped SrFeO_{3-δ} electrocatalysts and we investigated the effect of polyethylene glycol (PEG) addition as a secondary fuel on their structural, microstructural, redox and electrochemical properties. The perovskite-type powders were characterized by X-ray diffraction coupled with Rietveld refinement, scanning, and high-resolution transmission electron microscopies, thermogravimetric analysis, nitrogen adsorption measurements, and temperature-programmed reduction. Electrical conductivity and overpotential measurements were performed after the deposition of the powders onto a Gd-doped ceria electrolyte pellet. Stable high-valence B-site cations were detected in the powders prepared from sucrose-PEG fuel mixtures, although a substantial improvement of the conductivity and a decrease of the overpotential values were obtained only with high molecular weight PEG. The superior electrochemical performance obtained using PEG with high molecular weight has been ascribed to a faster interaction of the powder with the oxygen gas phase favored by the nanometer-sized crystalline domains.

Keywords: doped strontium ferrate; fuel effect; solution combustion synthesis; sucrose-assisted combustion; solid oxide fuel cells; cathode materials; polyethylene glycol

1. Introduction

Solution combustion synthesis (SCS) is a convenient synthesis route to obtain perovskite-type materials [1–4]. In SCS, a fast heat-induced chemical chain reaction propagates through a gel network between the oxidizing agents, namely metal nitrates (which represent also the source of metal cations), and the reducing organic molecules (fuel) with chelating properties towards the metal cations [2]. Among the SCS tunable parameters, the fuel type needs to be properly chosen in order to prepare materials with targeted properties [1,2,5]. In particular, the fuel-type can affect phase composition,

morphology, surface charge, oxidation states of the component elements, thermal stability, and electric-magnetic characteristics of the obtained materials [5,6]. Besides having reducing, chelating, and templating functions, an important feature of the fuel to be taken into consideration is its eco-friendly nature: Preferred SCS fuels are inexpensive, easy to handle, and with a limited environmental impact [2].

Sucrose is an example of eco-friendly fuel and sucrose-assisted SCS has been successfully employed in the literature for the synthesis of mixed oxides [7–10]. It is able to form chelates with most of the metal cations, it has a noticeably high reducing power and it is able to modulate the morphology and texture of the material. For example, Aliotta et al. [7], regarding the SCS of $\text{Ce}_{0.8}\text{Sm}_{0.2}\text{O}_2$, hypothesized that sucrose is able to form a gel network where metal cations remain trapped in sucrose-metal cation agglomerates, with a positive effect on the porosity, grain growth, and densification of the powders. This specific template function of sucrose has been reported as well by other authors, highlighting that, by using sucrose as a fuel, high surface area powders with low agglomeration degrees are produced [7,8,10–13]. Sucrose is often used to create a reducing environment around a metal cation and govern oxidation states [14]. As an additional advantage, in most cases, the use of sucrose allows the combustion reaction to occur without adding ammonia as a pH regulator, which is necessary in the case of traditional citric acid fuel [13]. However, sucrose-assisted combustion has also some drawbacks: The amount of residual carbon is large and the excessive increase in the volume of the light-weight as-burned powder causes powder loss outside of the reaction vessel [2].

PEG, a multifunctional polyether compound, is another eco-friendly fuel, often used, alone or mixed with other organics, as a structure-directing agent and/or solvent in sol-gel synthesis [15–18]. It has been found that the variation of its molecular weight (MW) can modulate the microstructure and porosity development of the produced material [16,18–20].

The mixed-fuels approach in SCS was demonstrated to positively affect the electrocatalytic performance of perovskite-type materials in the oxygen reduction up to an order of magnitude [5,21–23]. PEG (MW = 20,000) was already employed in the compresence of sucrose in two previous papers dealing with $\text{Ba}_{0.5}\text{Sr}_{0.5}\text{Co}_{0.8}\text{Fe}_{0.2}\text{O}_{3-\delta}$ powders as cathodes for solid oxide fuel cells prepared by SCS [22,24]. Optimal features and electrochemical properties were reached by a mixture of sucrose and PEG in a 1:2.5 molar ratio [22]. The addition of PEG is effective in extending the chelating ability toward metal cations and the global efficiency of the combustion process, without altering too much the reduction power of the mixture [22]. The use of the two fuels allowed achieving high reducing power and high interaction of the fuel mixture with metal cations, favoring the stabilization of Co^{2+} reduced state in $\text{Ba}_{0.5}\text{Sr}_{0.5}\text{Co}_{0.8}\text{Fe}_{0.2}\text{O}_{3-\delta}$ structure. The obtained oxygen vacancy-rich configuration positively affected oxygen mobility and cathodic performance [22,24].

Perovskite-type compounds with ABO_3 structure are a well-known class of functional materials with a wide range of applicability in catalysis, electronics, optics, piezoelectrics, and other technological fields [25–27]. The perovskite structure formation depends on the relative A-site and B-site cation radius according to the Goldsmith tolerance factor, which is the most widely recognized criterion [28]. Electrocatalysts with ABO_3 structure found application as electrode materials for electrochemical devices like Intermediate Temperatures Solid Oxide Fuel Cells (IT-SOFC) [29–34], Symmetrical Solid Oxide Fuel Cells (SSOFCs) [35–37], and electrolyzers [35,38,39]. The main requirements of electrode materials are (i) to be able to adsorb oxygen from the air and catalytically reduce it (oxygen reduction reaction) or to evolve oxygen and catalytically oxidize the fuel (oxygen evolution reaction), (ii) to possess high mixed ionic and electronic conductivity, (iii) to be highly compatible with the electrolyte in terms of thermal expansion coefficient (TEC), to avoid detrimental effects on the performances and failures in long-term operations.

$\text{SrFeO}_{3-\delta}$ is a perovskite-type mixed oxide where iron has the expected oxidation state of +4, whereas in most ABO_3 perovskites, like pure and doped LaFeO_3 , the common oxidation state at B-site is +3 [38]. This compound is able to accommodate a large range of oxygen deficiencies, so that some Fe^{3+} , with a larger ionic radius, is formed to restore the electroneutrality [40,41]. The oxygen

non-stoichiometry is an important factor to achieve high oxygen adsorption, oxygen mobility, and high ionic conductivity [41,42]. Doped SrFeO₃ has been also studied as anodes and as electrodes in electrolyzers due to their high stability in both oxidative and reductive environments [43].

It has been already reported that Cerium doping at the A-site of the Strontium Ferrates stabilizes the perovskite cubic structure, with a solubility of about 15 mol% [40,44–46]. Cubic symmetry has been found to enhance the ionic conductivity with respect to less symmetric structures as it maximizes the overlapping between the 2p-orbitals of oxygen and d-orbitals of the transition metals at the B-site [47]. The oxygen deficiency δ and the average valence state of B-site cation decrease by increasing cerium concentration. It was also found that Cerium addition decreases the thermal expansion coefficient, making it closer to that of a classical Gd-doped CeO₂ electrolyte [48]. Otherwise, when cobalt replaces iron in the B-site of SrFeO_{3- δ} , the electronic conductivity improves, thanks to the intrinsic property of Co, as well as the ionic conductivity [49]. In addition, by introducing Cobalt as dopant, the lattice constant gradually decreases, limiting the distortion of the cubic structure [50]. Cobalt-containing cathodes are known for their good electrochemical performances at low-intermediate operating temperatures (20–700 °C) because of their excellent activity in the oxygen reduction reaction [38,51–53]. However, Cobalt-containing cathode materials exhibit high TEC values caused by the spin-state transition associated with Co³⁺ formation, leading to a mismatch with the electrolyte and a consequent thermomechanical instability of the electrochemical cell [54]. The higher cost of cobalt itself further limits the Co amount in the electrode formulations, encouraging new strategies leading to a good compromise between efficiency and stability [55].

Cerium and/or Cobalt-doped SrFeO_{3- δ} perovskite-type oxides have been already studied as cathode materials for IT-SOFCs [40,48,56], or oxygen membranes [46], although they have lower performance than the most commonly used LaFeO₃ [57]. Doped SrFeO₃ has been prepared by solid-state synthesis as well as by SCS starting from citric acid as a fuel, but they have never been prepared by using sucrose-assisted SCS.

In this work, Cerium and Cobalt-doped SrFeO₃ powders, with nominal composition Sr_{0.85}Ce_{0.15}Fe_{0.67}Co_{0.33}O_{3- δ} (SCFC), are produced for the first time by SCS assisted by sucrose (SCFC-S) or sucrose-polyethylene glycol (PEG) mixtures, by using PEG with different molecular weight, i.e., 1,000 (SCFC-SP1) and 20,000 (SCFC-SP20). The target was to find new correlations between the use of the PEG as a secondary fuel and the structure, redox behavior, texture, morphology, and electrocatalytic performance of the selected perovskite-type compound. The effect of two different PEG molecular weights was also investigated.

The most remarkable conclusion is that the addition of high molecular weight PEG to the sucrose primary fuel leads to an improvement of both oxygen reduction and evolution processes. This improvement was ascribed to the low-temperature formation of high valence iron and the presence of nanostructured crystalline domains, which enhance the oxygen exchange rate in the perovskite-type electrocatalysts.

2. Results and Discussion

2.1. The Combustion Process

The combustion process which took place during the synthesis of Sr_{0.85}Ce_{0.15}Fe_{0.67}Co_{0.33}O_{3- δ} (SCFC) was relatively fast and intense for all the investigated samples. The efficiency of the process, in terms of energy/time consumption, was measured by a thermocouple inserted in the reaction medium and quantified by the temperature/time profiles displayed in Figure 1. In particular, three parameters were chosen to quantify the combustion efficiency: The maximum temperature of the combustion peak, the combustion duration (connected with the width of the peak), and the ignition temperature, defined as the lowest temperature at which the mixture takes fire and continues to burn (Figure 1). High maximum temperatures, short duration, and low ignition temperatures commonly denote a great efficiency of the combustion process [2]. In Figure 1, the maximum temperature increases from 480 °C for SCFC-S to 605 °C for SCFC-SP20. The combustion duration decreases in the same direction

from 78 s to 38 s, whereas the ignition temperature from 184 °C to 133 °C. Therefore, the association sucrose-PEG, particularly for the highest PEG molecular weight, results in producing a more efficient combustion process (Figure 1).

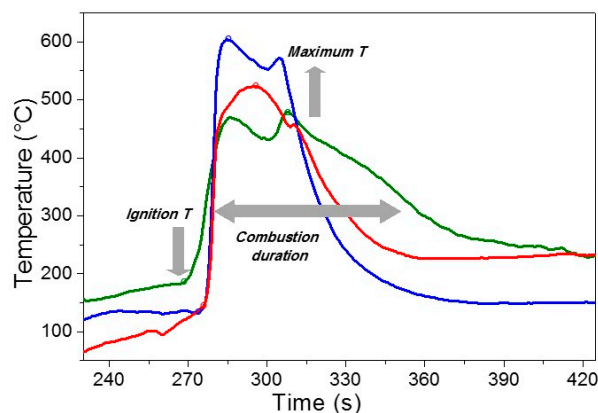


Figure 1. Temperature-time profiles registered during the combustion process of the three investigated samples, SCFC-S (green), SCFC-SP1 (red), and SCFC-SP20 (blue).

To explain these differences, it is worth to recall that the fuel has a triple function in the combustion mixture, i.e., to be reducer, complexing and microstructural templating agent. According to the propellant chemistry principles, the total reducing power of the PEG-containing fuel mixtures is slightly higher than that related to the sucrose single fuel system and this might account for the higher intensity of the process, as well as the stronger fuel-to-metal cations interaction. As pointed out in the literature [18,58,59], PEG 20,000 has a stronger interaction with metal cations than PEG 1000 and actually causes a more intense combustion process.

2.2. Structure and Microstructure of the Powders

Structure and microstructure of the samples were studied by X-ray powder Diffraction combined with Rietveld refinement. The graphical Rietveld refinements of the three powder patterns are reported in Figure 2a–c, with the respective enlargements in the 22–35° 2 θ region (d–f). Furthermore, the main structural and microstructural parameters are summarized in Table S1, together with the corresponding standard deviations obtained from Rietveld analysis. The powder prepared from sucrose single fuel is a single perovskite phase, whereas about 2 wt. % of CeO₂ were detected outside the perovskite structure in both the materials obtained from mixed fuels (Figure 2e,f and Table S1). According to the phase composition reported in Table S1, it was calculated that in SCFC-SP1 and SCFC-SP20 the amount of Cerium entering the perovskite structure is about 13 mol%, which is 2 mol% lower than the nominal composition (15 mol%). The structure symmetry of the perovskite-type phase, present in all the examined patterns, is cubic (Pm-3m), in agreement with the ICDD reference pattern of a Cobalt-doped SrFeO₃ compound with very similar B-site composition (SrFe_{0.7}Co_{0.3}O₃-PDFCard-04-016-4583). Partial A-site substitution of Strontium by Cerium cations in the perovskite systems under study resulted in a smaller cubic cell parameter, namely 3.866 Å, instead of 3.870 Å found for the above-mentioned reference composition. This is probably due to a charge compensation of iron and cobalt cations at the B-site. However, the cell parameter is in perfect agreement with the Cobalt-doped SrFeO₃ compound with an identical chemical composition (prepared with citric acid as fuel) recently published as a new entry in the ICDD database (GIA-Grant In Aid-2018-2019-I cycle-Editorial number: I08994). Cell parameters of the three samples are comparable within the experimental standard deviation calculated by the Rietveld program and according to the equal nominal composition of the powders (Table S1), suggesting that the cations inside the three perovskites have equipollent oxidation states. The major differences among the samples are observable in terms of microstrain, whereas the change in crystal

size is not dramatic. In particular, the highest microstrain values were registered for the two SCFC-SP1 and SCFC-SP20 powders.

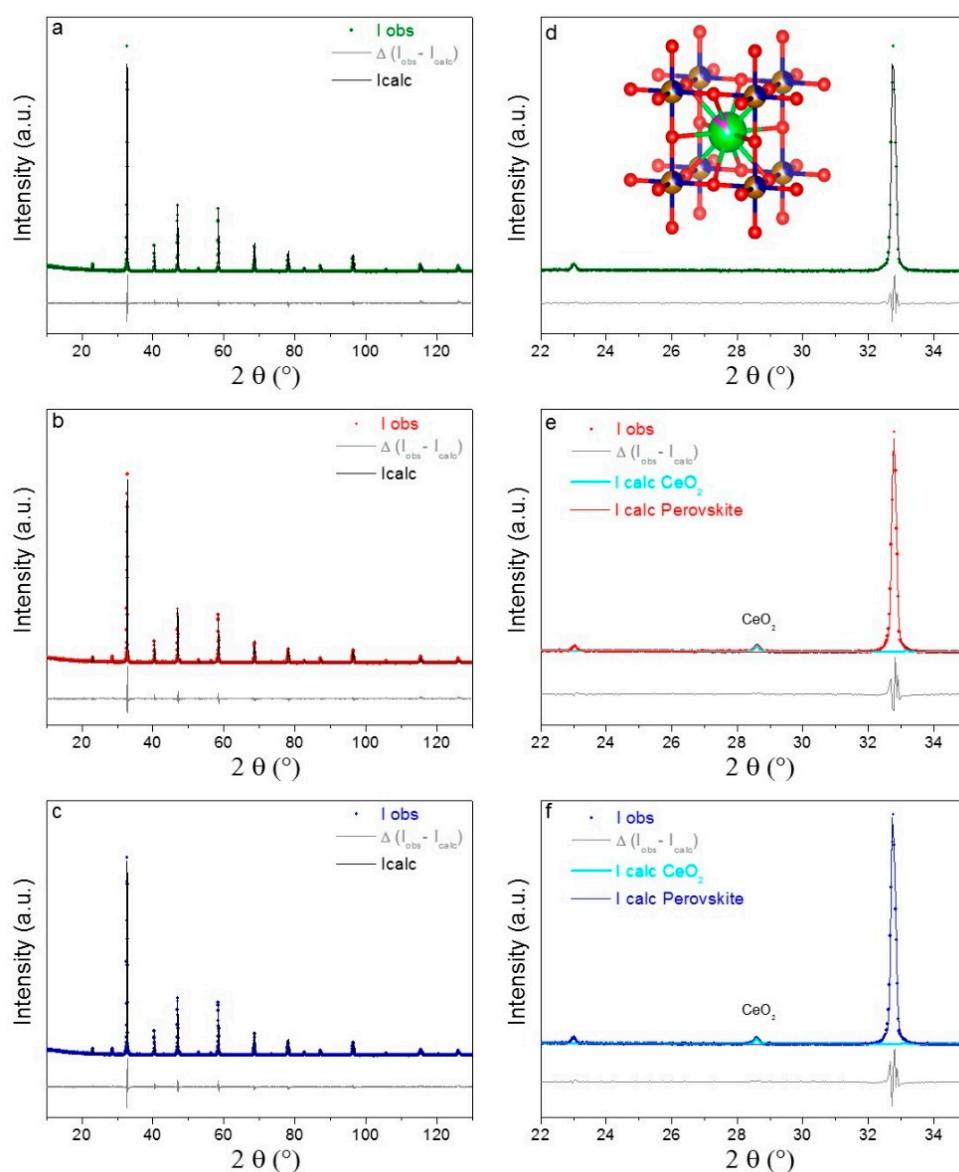


Figure 2. (a–c) Graphical Rietveld refinement of XRD patterns for the three examined samples; (d–f) enlargement of the graphical Rietveld fit in the angular range 22–35° with image of the refined perovskite structure in d (Sr and Ce are green and pink, Fe and Co are gold and blue, O is red) and indication of the CeO_2 phase formation in e and f.

Based on these outcomes, the different fuel-to-metal cation interactions and intensity of the combustion process, provoked by different fuels, influences the composition as well as the structural and microstructural properties. Indeed the addition of PEG seems to hinder the cerium entering the perovskite (Figure 2), whereas sucrose as a single fuel favors the cerium introduction in the perovskite framework if compared with citric acid [45]. Ce^{3+} introduction in the iron perovskite forces the Fe^{4+} -to- Fe^{3+} reduction process to compensate for the charge increase. Therefore, cerium oxide segregation in the samples prepared from sucrose-PEG mixtures is probably due to the hindering of this process caused by the high stability of B-site species with a high oxidation state (see Section 2.5). No segregated cobalt-containing compounds are detectable as cobalt enters the B-site of the ABO_3 perovskite very easily, in agreement with the literature [48,60]. Concerning the crystal size values

(Table S1), they are the result of a compensation between a stronger combustion process (in terms of the maximum temperature parameter), which promotes the crystal sintering, and a shorter process duration, which limits the crystal sintering. The higher microstrain values found for SCFC-SP1 and SCFC-SP20 might account for the 1.7 wt% CeO₂ segregation, causing a slight charge imbalance in the structure (Figure 2b,c). A very small fraction of Cobalt probably moved into segregated CeO₂, as demonstrated by the slight decrease of the cell parameter of CeO₂ from 5.411 (ICDD PDF card n° 00-004-0593) to 5.4099 ± 0.0004 Å (for SCFC-SP1) and 5.4078 ± 0.0005 Å (for SCFC-SP20), in agreement with what has been reported in the literature for cobalt-ceria systems [61].

2.3. Textural Properties of the Powders

Figure 3a displays the N₂ adsorption/desorption isotherm (type IV) of one of the samples, namely SCFC-SP20, as a representative example, whereas in Table S2 the textural parameters of all the samples are reported. The isotherm of Figure 3a has a very small hysteresis at relatively high pressures ($p/p_0 = 0.9$), typical of SrFeO₃-based powders with low mesoporosity [45]. All the examined powders have low surface area values, comprised between 20 and 29 m²/g (Table S2). Inside this range, results reported in Table S2 point out a clear decrease of porosity and surface area for the samples prepared from mixed fuels, whereas the pore dimension increases with PEG addition to sucrose primary fuel, in agreement with the literature [18]. The pore distribution of the same representative sample, SCFC-SP20, is reported in Figure 3b, evidencing two pore size regions. The main porosity is in the range 2–10 nm, whereas another minor contribution extends up to 35 nm (Figure 3b). This is in agreement with the presence of hysteresis at high pressures (Figure 3a) and with the morphological features reported in the next paragraph (Figure 4a).

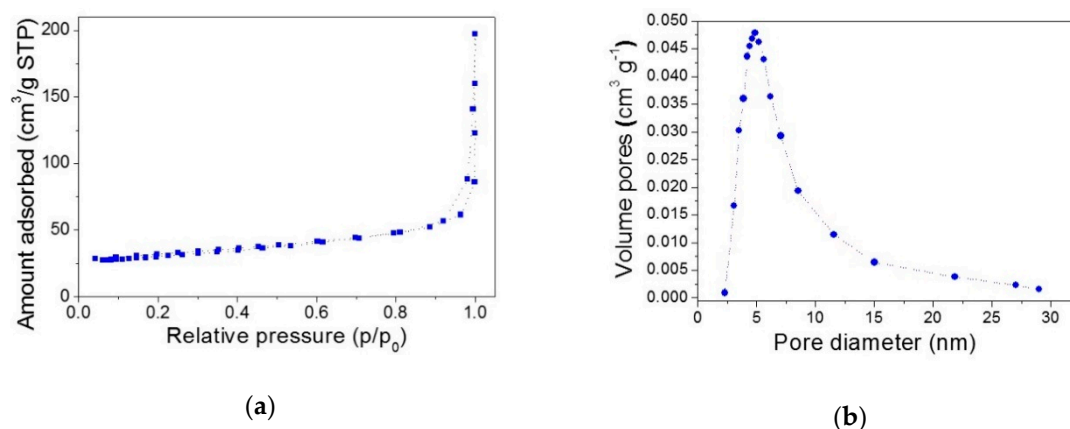


Figure 3. N₂ adsorption/desorption isotherm (a) and pore size distribution (b) of SCFC-SP20 as a representative sample.

A value for the grain (d_{BET}) was also calculated from N₂ adsorption data by using the well-known relationship between the surface area (S_{BET}) and grain size, i.e., $d_{\text{BET}} = 6/\rho \times S_{\text{BET}}$ [62], where the density ρ was obtained by the Rietveld Refinement for this structure (5.769 g/cm^3). From d_{BET} , it was possible to obtain the agglomeration degree, calculated as the ratio between the crystal size obtained from the XRD and the grain size obtained from N₂ adsorption (Table S2). A mean value of 3 agglomerated crystallites form the mean grain of SCFC-SP1 and SCFC-SP20 powders, whereas 2 agglomerated crystallites form the mean grain of the SCFC-S powder. As also discussed in the next paragraph, a stronger agglomeration occurs in SCFC-SP1 and SCFC-SP20 (Table S2).

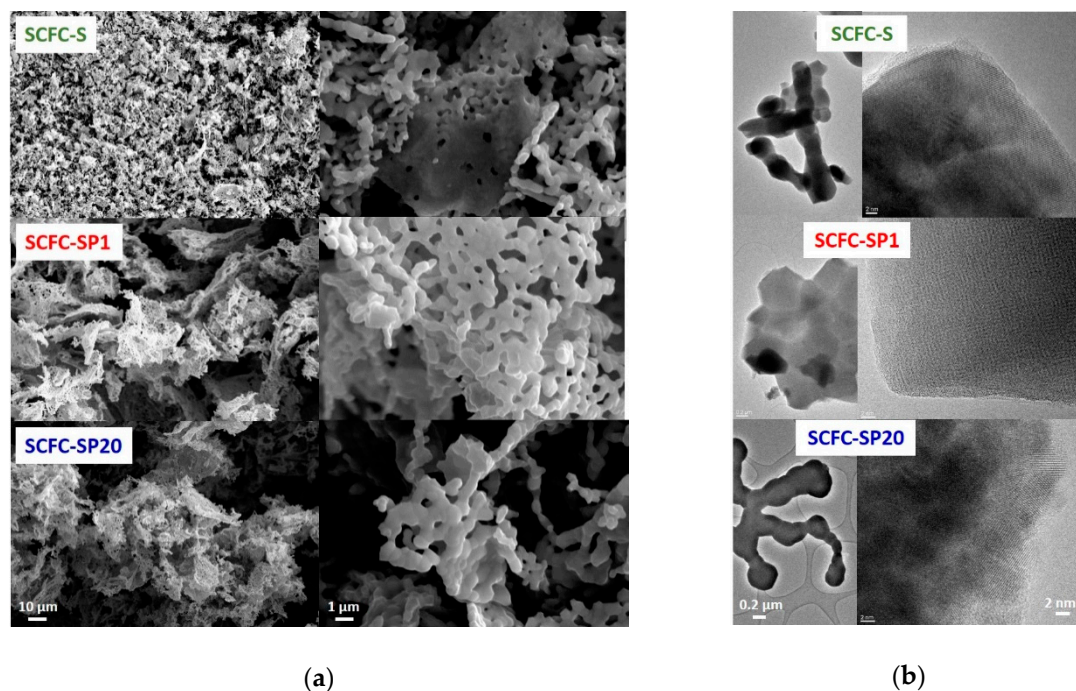


Figure 4. (a) SEM; (b) TEM.

2.4. Morphological Properties of the Powders

A selection of images obtained by electron microscopy techniques is shown in Figure 4. SEM analysis (Figure 4a) indicates the presence of flake-shaped aggregates composed by irregular sub-micrometric spherical-like particles, forming void inter-particle space. The sintering of the primary particles can be clearly evidenced. The agglomerate size appears more regular in the powders prepared from mixed fuels. In Figure 4b TEM micrographs evidence the presence of different particle aggregates at the nanometric scale, mostly roundish although some sharper edges are observable. All systems resulted in extensively crystalline structures, although the crystalline fringe systems are more extended in the order SCFC-SP20 < SCFC-S < SCFC-SP1. The agglomeration degree values reported in Table S2 agree with the diameter observed in Figure 4a for SCFC-S (600–1000 nm) and for SCFC-SP1 and SCFC-SP20 (600–2400 nm). Therefore, the addition of PEG to the combustion mixture helps to produce a more regular grain size distribution at the expense of a slightly higher agglomeration. The analysis of the fringe patterns confirmed that in all three samples there are reflections at 2.70, 2.20, and 1.95 Å that are easily attributable to the $\text{Sr}_{0.85}\text{Ce}_{0.15}\text{Fe}_{0.67}\text{Co}_{0.33}\text{O}_{3-\delta}$ perovskite, in agreement with the reflection obtained from the XRD pattern. Other reflections at 1.50, 2.41, 2.60, and 2.50 Å were also observed, probably due to other mixed phases, for instance, $\text{SrFe}_{12}\text{O}_{19}$ (reference card 01-080-1197) and CoFe_2O_4 (reference card 01-079-1744) formed as impurities in the materials and not visible in the diffraction patterns because they were only present in a very limited amount.

2.5. Redox Properties of the Powders

Temperature-programmed reduction experiments (TPR) give interesting information on the redox properties of powders containing reducible cations. In Figure 5, the TPR results of the examined samples are reported together with possible redox couples involved in the reactions, whereas the corresponding experimental H_2 consumptions are listed in Table S3. As expected by their identical nominal composition, all the samples show similar redox behavior and three main reduction phenomena are distinguishable (Figure 5). However, the shifts observed in the positions and intensity of the peaks in Figure 5 reflect some diversities in the chemical surrounding of the reducible cations.

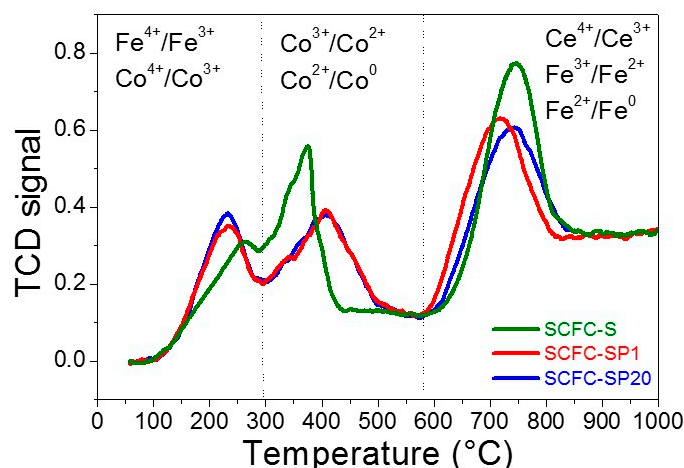


Figure 5. Temperature-programmed reduction experiment (TPR) results.

The reduction events in the low-temperature range (100–290 °C) can be ascribable to the presence of a certain amount of B-site cations with higher oxidation state, i.e., Fe^{4+} and Co^{4+} , as also observed by Carvalho et al., performing TGA experiments under H_2/N_2 flow on similar compounds with similar results [63]. The presence of Fe^{4+} is expected for a SrFeO_3 -based material, although the Fe^{4+} content decreases by Ce-doping [40].

In the middle-temperature region (290 °C–580 °C), Co^{3+} to Co^{2+} and Co^{2+} to Co^0 reduction processes occur. The theoretical H_2 consumption for the complete reduction of Co^{3+} to Co^0 is 60.5 mL H_2/g , assuming that all the cobalt in the sample was present as Co^{3+} . This value is about 20% higher than the values registered for the 3 samples under study (Table S3), indicating that not all the cobalt is found in the 3+ oxidation state.

In the high-temperature region (580 °C–1000 °C), Fe^{3+} to Fe^{2+} and Fe^{2+} to Fe^0 reduction occurs together with the Ce^{4+} to Ce^{3+} reduction according to previous work [40]. Based on the nominal composition $\text{Sr}_{0.85}\text{Ce}_{0.15}\text{Fe}_{0.67}\text{Co}_{0.33}\text{O}_{3-\delta}$ and assuming that in the high-temperature range all the iron is in the 3+ oxidation state, the theoretical H_2 consumption for the complete reduction of Fe^{3+} to Fe^0 is 122.8 mL H_2/g . In addition, if all the cerium in the sample was present as Ce^{4+} , the theoretical H_2 consumption for the complete reduction of Ce^{4+} to Ce^{3+} would be 9.2 mL H_2/g . Therefore, the theoretical high-temperature H_2 consumption should be the sum of these contributions, i.e., 132.0 mL H_2/g . However, looking at Table S3, none of the samples consumes such amount of hydrogen in the high-temperature range. For example, in the case of SCFC-S, the high-temperature consumption of H_2 is about 9% smaller than the theoretical one (121.0 vs. 132.0 mL H_2/g). This apparent discrepancy is due to the incomplete Fe^{2+} to Fe^0 transformation, as observed for Ce-doped SrFeO_3 in a previous study [40].

In the case of SCFC-SP1 and SCFC-SP20 powders, a higher percentage of highly oxidized species is registered with respect to SCFC-S, at the expenses of the Fe^{3+} and Co^{3+} species (Figure 5 and Table S3). In addition, the signals SCFC-SP1 and SCFC-SP20 in the 580–1000 °C temperature range are slightly shifted and reduction occurs at lower temperatures for SCFC-SP1, indicating that reducibility of Fe^{3+} is favored for this sample. The presence of Fe^{4+} in the perovskite structure should cause the contraction of the cell parameter/volume due to the smaller ionic radius of Fe^{4+} with respect to Fe^{3+} , but the crystal cell sizes of the three materials before the TPR experiments (reported in Table S1) are very similar. This suggests that high oxidation state cations are probably formed during the TPR pre-treatment, in agreement with the TGA results discussed later. Actually, in this perspective, the SCFC-SPx powders seem more susceptible than SCFC-S to be oxidized at T lower than 500 °C (during the sample pre-treatment).

Total hydrogen consumption values reported in Table S3 are comparable. The slightly smaller values registered for SCFC-SP1 and SCFC-SP20 are ascribable to the incomplete reduction of bulk

CeO₂, present in these samples as segregated phases. In fact, Ce⁴⁺ reduction in the bulk CeO₂ can occur at T > 1000 °C, although it already starts at T < 1000 °C.

Another important factor for a good electrode performance is represented by the presence and amount of oxygen vacancies as carriers of O₂[−] and responsible for ionic conduction. Thermogravimetric analysis was performed by saturating the strontium ferrate with oxygen and subjecting it to thermal treatment under inert gas flow (see Materials and Methods section). The mass loss during this thermal treatment is linked to the released oxygen and indicates the capability of the material to entrap oxygen in its vacancies. Two different thermogravimetric procedures were adopted in this work, to evaluate the influence of the pre-treatment on the oxygen capture/release, as reported in the Materials and Methods section). In the first procedure, called here as “single step,” the mass loss of the sample is measured under nitrogen at increasing temperatures. In the second procedure, called here as “multistep,” the sample is subjected to different redox treatments under different conditions and the mass loss was followed during all these steps. In Figure 6a, TGA profiles obtained by pre-treatment in N₂ are reported. The percentages of the total oxygen release calculated as weight loss are 2.6% for SCFC-S, 1.7% for SCFC-SP1, and 2.2% for SCFC-SP20. In these experimental conditions, oxygen vacancies are mostly abundant in SCFC-S whereas they are very limited in SCFC-SP1. In all cases, the differences are significant because always higher than the standard deviation (±5 wt%). Looking at Figure 6a, the first weight loss occurring up to 450 °C is ascribable to the presence of α-O₂, namely mobile oxygen (strictly related to the vacancies), whereas over 450 °C also lattice oxygen β-O₂ can be released.

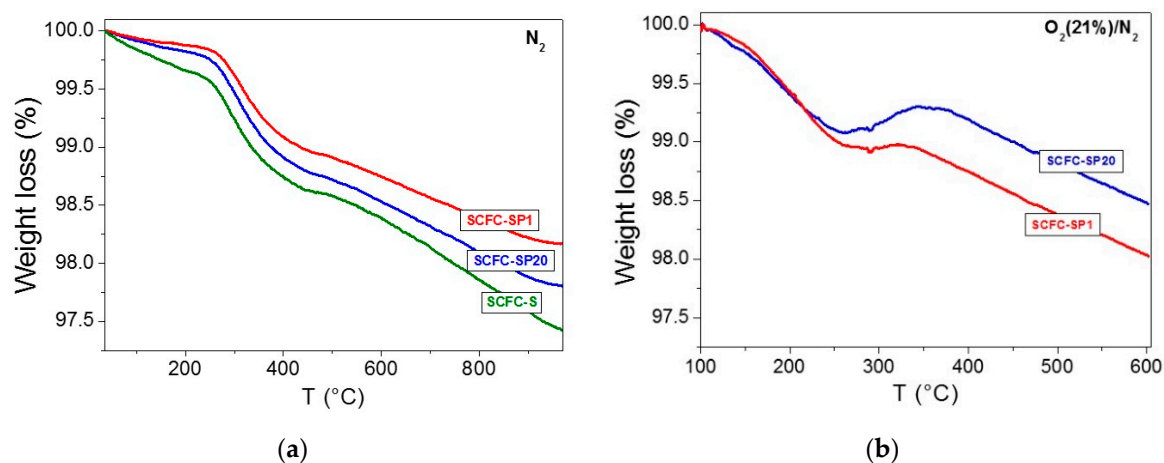


Figure 6. (a) Thermogravimetric analyses (TGA) under N₂ flow; (b) TGA under O₂ (21%)/N₂ flow (step 3 of Figure S1).

It is worth knowing that a mass quadrupole, positioned downstream of the thermal treatment for monitoring gaseous species evolution, allowed detecting a relevant amount of CO₂ released from SCFC-SP20 during the pre-treatment. It is supposed that the observed CO₂ evolution is due to the presence of oxygenated organic residues in the materials, probably derived from incomplete combustion of PEG. The same residues are probably responsible for the surface area decrement observed in this sample (Table S2), in agreement with the literature [64,65].

The multistep TGA procedure, whose step 3 is reported in Figure 6b, is particularly relevant as it can describe the redox behavior of a powder subjected to isothermal and non-isothermal oxidation-reduction cycles (see Materials and Methods). Similar experiments have been already used in the literature for other systems [7]. The complete series of steps followed by this TGA procedure and the relative weight losses are reported in Figure S1. Both the samples have a higher tendency to be reduced than oxidized at 600 °C (compare step 5 and step 6 in Figure S1). However, SCFC-SP20 shows a larger tendency to be oxidized at low temperatures than SCFC-SP1 (Figure 6 and Figure S1-step3). This means that highly oxidized B-site species are stable at low temperatures, and their stability is higher in SCFC-SP20. It is worth to remind that in the same sample the stronger interaction of the gel

network with metal cations during the synthesis process produced a very peculiar morphology. These results might have an importance during the operations of the electrochemical device, where materials operate under frequent oxidation-reduction cycles. Furthermore, Figure 6b confirms that highly oxidized species were formed during the short oxidative pre-treatment before the TPR experiment, highlighting the importance of the sample pre-treatment, able to influence the ability of the materials to interact, adsorb and desorb oxygen under specific experimental conditions. This is the first time that a clear correlation between the redox behaviors and the electrocatalytic performance of a material can be assessed, thanks to the type of multistep TGA experiment carried out. So far, the complexity of the phenomenon hampered the definition of any kind of correlation. For instance, the morphology observed in Figure 4b can be responsible for the increased reactivity of this sample toward the gas phase at T below 500 °C. This is in agreement with the results of Royer et al. [66], who evidenced the important role of morphology in the oxygen-involving processes for a perovskite exploited for CH₄ and CO oxidation. Furthermore, in the same literature paper, it was highlighted that the capacity of oxygen desorption or the cations reducibility could be well correlated with the catalytic activity only by taking into account as well the specific conditions of the catalytic tests and of the sample pre-treatment [66].

2.6. Electrochemical Properties of the Powders Deposited on the Electrolyte in Half-Cell Configuration

The electro-catalytic performances of the above-characterized samples were tested and a commercial LSCF cathode from Praxair, Inc. was used as a reference ($\text{La}_{0.6}\text{Sr}_{0.4}\text{Fe}_{0.8}\text{Co}_{0.2}\text{O}_{3-\delta}$, 100% cubic perovskite, surface area 11.19 m²/g). Figure 7 reports the overpotential measurements of specimens evaluated at 600 °C (a) and 800 °C (b).

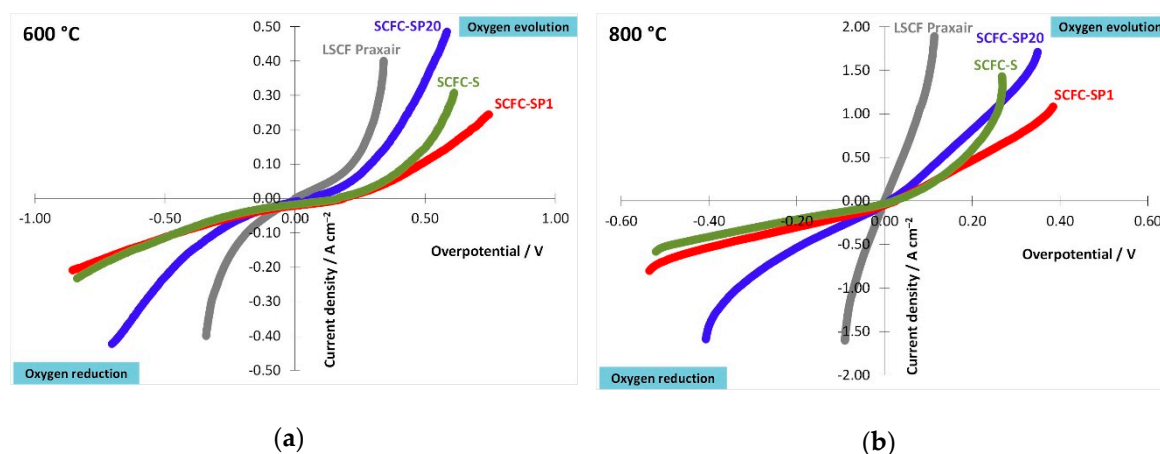


Figure 7. Overpotential measured at 600 °C (a) and 800 °C (b) for the three samples under study in comparison with a reference LSCF perovskite (Praxair).

All samples show asymmetrical trends in oxygen reduction and evolution, whereas the highest symmetry is shown by the commercial LSFC. Among the three samples under study, SCFC-SPx has a higher symmetrical behavior than SCFC-S and SCFC-SP20 is the most symmetrical one. Therefore, oxygen evolution is slightly favored in comparison with the oxygen reduction and this indicates a good behavior of the materials also as anode for IT-SOFC, as highlighted in the literature [37,43,67]. The commercial specimen shows the highest performances with the lowest overpotentials achieved i.e., -0.4 A cm^{-2} at -0.34 V for the reduction reaction and 0.4 A cm^{-2} at 0.34 V for the evolution reaction of oxygen (Figure 7a). However, it must be considered that both chemical composition and structure of LSCF Praxair are different from the perovskites investigated in this work. The overall best performance was achieved by SCFC-SP20 and the worst one by SCFC-SP1, with a maximum difference of half order of magnitude. This result indicates that the local environment of the cations plays a fundamental role in the electrochemical performance of cathode materials, although all the samples have the same chemical composition. In Figure 7b, the overpotential curves evaluated at

800 °C are depicted. A significant asymmetric behavior towards oxygen evolution and reduction reactions is observed at 800 °C for both SCFC samples and LSCF Praxair. In particular, a significant propensity at high current density towards the evolution of oxygen is reached. This indicates that, in this mechanism, an important role may be played by the oxygen storage capability of the materials under investigation. In particular, SCFC-S improves at high currents, since the oxygen diffusion is easier because it has more charge carriers, as demonstrated by TGA results (Figure 6a), but far from the zero current point is worse because it is more resistant (see also Figure 8 and discussion). Therefore, also in these conditions (800 °C), SCFC-SP20 possesses improved performances with respect to the other two electrocatalysts. In Figure 8, results about conductivity (σ) are reported (Arrhenius plots).

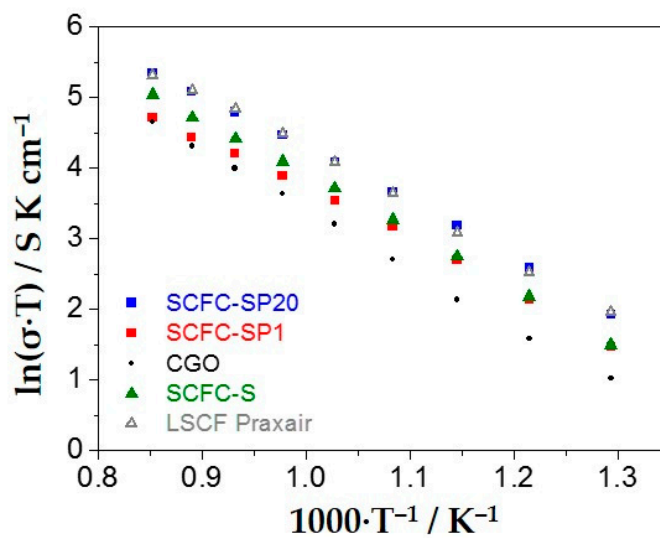


Figure 8. Electrical conductivity (Arrhenius plots) of the three samples under study in comparison with a reference LSCF Praxair perovskite.

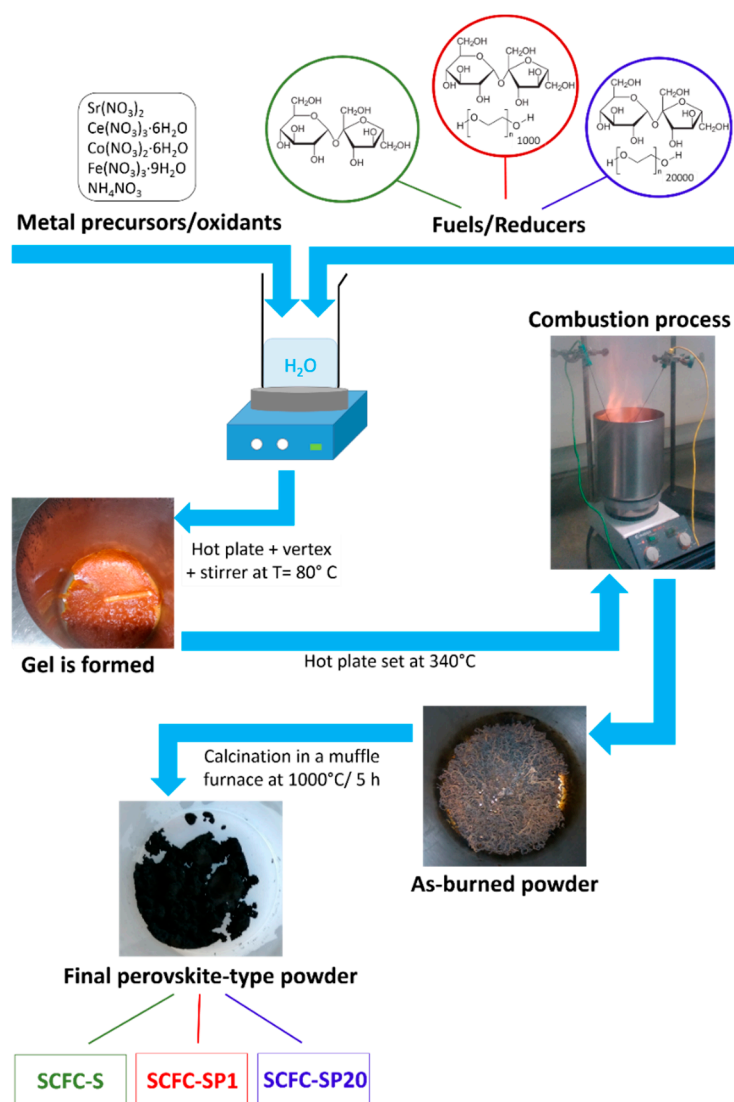
Coherently with overpotential measurements, SCFC-SP20 demonstrated the highest conductivity and similar behavior to Praxair LSCF, whereas the worst performance was observed for SCFC-SP1, especially at high temperatures. It can be concluded that SCFC-SP20 electrochemical behavior is superior because it is more conductive. Its higher electrical conduction can be ascribed to two main factors: Its ability to stabilize Fe^{4+} and its peculiar morphology, which favors the oxygen exchange with the gas phase, both in the reduction and evolution reactions (Figure 4b). On the other hand, in our particular case, porosity of the powder before the deposition onto the GDC electrolyte does not seem to play a role in the cathode electrochemistry, considering that the most porous powder, SCFC-S, is not the one with highest electrical conductivity (compare Table S2 with Figures 7 and 8).

The Arrhenius plot reported in Figure 8 indicates that SCFC-SP1 and SCFC-S were activated by the lowest (0.63 eV) and the highest (0.73 eV) energy values, respectively, whereas SCFC-SP20 has an intermediate activation energy value (0.70 eV), similar to the GDC electrolyte (0.71 eV), and LSCF Praxair has an activation energy of 0.66 eV. Activation energy values are directly related to the oxygen vacancies mobility more than to the amount of oxygen vacancies itself. Therefore, it is postulated that a higher oxygen vacancies mobility is attained by the sample with the smallest amount of oxygen vacancies (see Figure 6a), where vacancy clustering is less probable. Vacancy clustering has been already observed in the literature for similar perovskite-type compounds [68].

3. Materials and Methods

3.1. Powders Preparation

Scheme 1 describes the procedure used for the synthesis of the powders.



Scheme 1. Procedure used for the solution combustion synthesis of the three investigated samples.

The same general procedure was used for the preparation of mixed oxide powders of $\text{Sr}_{0.85}\text{Ce}_{0.15}\text{Fe}_{0.67}\text{Co}_{0.33}\text{O}_{3-\delta}$ composition (SCFC), irrespective of the fuel. 1.7958 gr of $\text{Sr}(\text{NO}_3)_2$ (anhydrous, $\geq 99.97\%$ Alfa Aesar GmbH & Co KG, Kalsruhe, Germany), 0.6503 gr of $\text{Ce}(\text{NO}_3)_3 \cdot 6\text{H}_2\text{O}$ (99.99%, Sigma-Aldrich & Co Saint Louis, MO 63103, USA), 0.9443 of $\text{Co}(\text{NO}_3)_2 \cdot 6\text{H}_2\text{O}$ (99.99% Sigma-Aldrich & Co Saint Louis, MO 63103, USA), and 2.7227 gr of $\text{Fe}(\text{NO}_3)_3 \cdot 9\text{H}_2\text{O}$ (99.99% Sigma-Aldrich & Co Saint Louis, MO 63103, USA) were carefully weighted in the required proportions to obtain about 2 g of final product, poured in a 1 L stainless steel beaker and dissolved in distilled water (200 mL) under magnetic stirring. Proper amounts of ammonium nitrate ($\geq 99.5\%$ BioXtra-Sigma-Aldrich Chemie GmbH, Schnellendorf, Germany) and sucrose (Eridania, Italia S.P.A, Bologna, Italy) were then added to the metal precursor solution as oxidant additive and propellant–template–complexant, respectively. Two powders were synthesized by adding polyethylene glycol at different molecular weights (PEG, MW 20,000 purum, Fluka Chemie, Buchs, Switzerland and PEG MW 1,000 Alfa Aesar GmbH & Co KG, Kalsruhe, Germany) as secondary fuels. Taking into account only the primary fuel, the fuel/metal cation molar ratio was set to 2.2, while the reducers/oxidizers ratio (Φ) was set to 2.1 (slightly over-stoichiometric). The water was left to evaporate from the precursor solution at the controlled temperature of 80°C under constant magnetic stirring until the formation of a homogeneous sticky gel. The combustion reaction was triggered and initiated by setting the hotplate temperature to around 300°C (real temperature was about 210°C). The as-burned powders were fired at higher

temperatures in a muffle furnace (1000 °C/5 h) for the crystallization of the perovskite-type phase and the elimination of any carbon residues derived from the combustion process. The sample prepared from sucrose is labeled SCFC-S and those synthesized from sucrose+PEG1000 or PEG20000 will be indicated as SCFC-SP1 and SCFC-SP20, respectively.

3.2. Physicochemical Characterization

The temperature–time profiles of the combustion process were recorded during the combustion process by means of a K-type thermocouple (1.5 mm in diameter) coupled with a data logger (PICO technology) with a sampling velocity of 20 bit per second and a computer with Picolog software.

X-ray diffraction (XRD) measurements were carried out on a Bruker-Siemens D5000 X-ray powder diffractometer equipped with a Kristalloflex 760 X-ray generator (Bruker AXS GmbH, Karlsruhe, Germany) and with a curved graphite monochromator using Cu K α radiation (40 kV/30 mA). The 2θ step size was 0.03, the integration time was 20 s per step, and the 2θ scan ranged from 10° to 130°. The powder diffraction patterns were analyzed by Rietveld refinement using the GSAS package [69]. As a starting model, we used a recently published reference structure with the same chemical composition but prepared by a different fuel type (GIA-Grant In Aid-2018-2019-I cycle-Editorial number: I08994). A Chebyshev polynomial function with 15 coefficients was chosen for the background and the Pseudo-Voigt function with the Finger, Cox & Jephcoat asymmetry correction was selected for the peak profile fitting. In the structure refinement lattice constants, Debye–Waller factors, microstrain, and the full width at half maximum (FWHM) were considered as variable parameters. From fitting results, the structural parameters of the investigated compounds and, in particular, phase composition and the relative cell edge lengths were obtained. An estimation of the crystal size values was obtained by the Scherrer equation in agreement with the GSAS package procedure. The agreement factors (R values), R_p , wR_p , RF^2 , and χ^2 were acceptable [70,71]. The standard deviation of the refined values for cell length, cell volume, mean crystal size, microstrain, and weight percentage of phase were obtained from Rietveld analysis and the values are reported in Table S2 and in the text along with the respective parameters. The obtained Debye–Waller factors for the perovskite-type phase are in good agreement with literature.

Specific surface area (SSA) measurements and pore texture analyses were performed using a Sorptomatic 1900 Instrument (Thermoquest Italia S.p.a., Milano, Italy), by physical adsorption/desorption of N₂ at the temperature of liquid nitrogen (−196 °C). The samples were pre-treated under vacuum at 250 °C for 3 h prior to the measurements. The specific surface area was calculated by applying the BET method to the adsorption branch of the isotherm in the standard pressure range of 0.05–0.30 p/p₀ [72]. By analysis of the desorption branch, using the BJH calculation method in the range 0.42 < p/p₀ < 0.98, the mean pore diameter and cumulative pore volume were obtained [73]. The total pore volume at p/p₀ = 0.99 (single point of desorption branch) was also quoted. The so obtained textural parameters were quoted with a precision of $\pm 10\%$.

SEM measurements were performed using a scanning microscope ZEISS EVO 50 XVP (Carl Zeiss AG, Oberkochen, Germany) equipped with a LaB₆ source and a secondary electron detector. The samples prior to the SEM investigation were sputtered with 20 nm of a gold layer to avoid charging effects using a Bal-tec SCD050 sputter coater (Leica Biosystems Inc., Buffalo Grove, IL, USA)

High-Resolution Transmission Electron Microscopy (HRTEM) was performed using a JEOL JEM. 3010UHR instrument (JEOL USA Inc., Peabody, MA, USA) working at 300 kV equipped with a single crystal LaB₆ source. The sample was dry-deposited on Cu “holey” carbon grids (200 mesh) for the analysis. With regard to the analysis of the fringe patterns, values of d_{hkl} were determined and consequently attributed to indexed reference patterns of database ICDD (PDF-2 software). All the powders were analyzed immediately after calcination treatment.

Reduction properties of the perovskite oxides were studied by temperature-programmed reduction (TPR) measurements. Experiments were carried out with a Micromeritics Autochem 2910 apparatus equipped with a thermal conductivity detector (TCD) (Micromeritics Instrument Corp., Norcross, Georgia, U.S.A.). Before starting the analyses, the catalyst (ca. 100 mg) was pre-treated flowing a 5%

vol O₂ in He gas mixture (30 mL min⁻¹) at 500 °C (10 °C/min) for 10 min to clean the surface and then cooling down in He flow (30 mL min⁻¹) up to room temperature. A 5 vol% H₂ in Ar gas mixture (30 mL min⁻¹) was used to reduce the sample by heating from room temperature to 1050 °C at the rate of 10 °C min⁻¹. The hydrogen consumption associated with the TPR profile was determined by applying a calibration curve.

Thermogravimetric analyses (TGA) were performed with a TGA/DSC1 STAR system (Mettler Toledo, Bristol, United Kingdom). Two types of experiment were performed by TGA:

(i) In the “single step” TGA experiment, the sample (10 mg) was pre-treated in N₂ (30 mL min⁻¹) at 750 °C for 1 h (step 1), then it was cooled down to room temperature in air (30 mL min⁻¹) (step 2) and purged with N₂ (30 mL min⁻¹) for 30 min (step 3). After that, the sample was again treated under N₂ (30 mL min⁻¹) by heating (rate 5 °C/min) from room temperature up to 1100 °C (step 4). Step 1 was performed to remove any adsorbed water, oxygen, or carbonate species; step 2 aimed to saturate all the vacancies with oxygen; step 3 aimed to eliminate all the physisorbed oxygen species; step 4, during which the removal of chemisorbed oxygen species occurred, was taken into account to evaluate the oxygen vacancies content of the sample. The evolution of gaseous species (CO₂, H₂O, O₂) occurring during the above steps was monitored by online mass quadrupole (Thermostar™, Balzers Instruments, Vaduz, Liechtenstein).

(ii) In the “multistep” TGA experiment, the sample (10 mg) was pre-treated under air (30 mL min⁻¹) by heating from 25 to 100 °C (step 1), holding at 100 °C under airflow for 30 min (step 2), in order to clean the surface and remove any water and CO₂ chemisorbed. After that, a sequence of 5 steps (step 3–7) carried out alternatively under oxygen and N₂, at a constant flow of 30 mL/min, was started with the aim to simulate the typical operating temperature and redox cycles experienced by an electrocatalytic material (Figure S1). In detail, the following steps were performed: The sample was heated from 100 to 600 °C (heating ramp 10 °C/min) under oxygen (step 3), holding time at 600 °C for 30 min (step 4), then at the same temperature the gas atmosphere was switched to N₂ for 30 min (step 5), and successively again to air for 30 min (step 6). Finally, under the same atmosphere, the sample was cooled down under oxygen flow from 600 to 100 °C (step 7).

3.3. Electrochemical Characterization

A potentiostatical frequency-response analyzer equipped with 20 A booster (Autolab PGSTAT30, Metrohm BV, Kanaalweg 29-G, 3526 KM Utrecht, The Netherlands) was employed and impedance spectra were obtained in the frequency range from 10 mHz to 1 MHz, at 0 V cell voltage and with an applied AC-voltage amplitude of 10 mV rms, using the same set-up, according to Dunyushkina et al. [74]. The experiments were conducted by using a three-electrode cell supported on a commercial Gadolinium-doped ceria (CGO, Ce_{0.8}Gd_{0.2}O₂, Praxair surface technologies, 1500 Polco Street, Indianapolis, IN 46222, USA) dense electrolyte pellet of 300 microns thickness. 2 mg cm⁻² of perovskite electrocatalyst were deposited in two different areas of both sides of the electrolyte, with a Pt electrode (MaTecK GmbH, Im Langenbroich 20, D-52428 Jülich, Germany) as a reference. After the deposition of the powder, a thermal treatment (1100 °C/2 h) under static air was carried out to ensure good adhesion between electrode layers and electrolyte. The temperature was controlled by a thermocouple (RS PRO) at a distance of 0.5 cm from the electrode. Electrochemical measurements were realized under static air in the range 400–900 °C.

Overpotential measurements were performed through current–voltage (I–V curve) experiments and considering the Ohmic constraint measured from the Electrochemical Impedance Spectroscopy (EIS) spectra carried out at the same temperature. A commercial LSCF (Praxair surface technologies, 1500 Polco Street, Indianapolis, IN 46222, USA) was also tested under identical experimental conditions as a reference material. For the electrochemical data analysis, two softwares supplied with the Autolab PGSTAT30 were used (GPES e FRA).

4. Conclusions

In this work, Cerium and Cobalt-doped SrFeO₃ powders as electrocatalytic materials were synthesized through the SCS assisted by a sucrose or sucrose—polyethylene glycol (PEG) mixtures, using PEG with different molecular weight. The use of several complementary characterization techniques allowed us to evidence the main features induced by the use of PEG and to identify some important synthesis-structure-properties relationships.

PEG addition limits the cerium solubility in the Co-doped SrFeO₃ through the stabilization of the highly oxidized B-site species, Fe⁴⁺ and Co⁴⁺. These cationic species are easily formed at about 350–400 °C under a moderately oxidative atmosphere. PEG with higher molecular weight is more efficient in the stabilization of such highly oxidized cations. In addition, it creates a peculiar environment favorable to improve the material activity, promoting the formation of powders with 200 nm crystallites and short crystalline domains of 5–10 nm, which are more effective in both the oxidation and reduction processes at the interface with the gas phase. Similar conductivity values were achieved by sample obtained by Sucrose-PEG 20000 fuel mixture in comparison with the commercial Sr and Co-doped LaFeO₃ sample. On the contrary, more extended crystalline domains are visible in the low molecular weight PEG-derived sample, whereas sucrose alone, with much less stabilization efficiency towards highly oxidized cations, does not produce materials with the best electrochemical performance, although it is able to produce higher surface area, porosity and oxygen-deficient powders.

Looking toward an optimization strategy of the cathode materials properties, these findings highlight that the synthesis parameters—and especially the nature of the fuel—have a primary role, on a par with the chemical composition. The obtained results established new connections between synthesis conditions, structure, microstructure–morphology–texture, redox behavior, and electrochemical properties, offering concrete strategies for the future optimization of the electrocatalytic materials.

Supplementary Materials: The following are available online at <http://www.mdpi.com/2073-4344/10/1/134/s1>, Table S1: Structural and microstructural parameters extracted from Rietveld Refinement of XRD data, Table S2: Textural parameters calculated from N₂ adsorption/desorption measurements, Table S3: Hydrogen consumptions (ml/g) per range of temperatures and total hydrogen consumption calculated from temperature-programmed reduction experiments, Figure S1: Experimental conditions used and weight loss variation in the second TGA experiment title.

Author Contributions: Conceptualization, F.D., M.L.T., M.L., and A.S.A.; methodology, F.D., M.L.T., G.M., L.F.L., and M.L.F.; validation, F.D., M.L.T., G.M., L.F.L., and M.L.F.; formal analysis, G.M., F.D., L.F.L., M.L.T., M.L.F., S.T., and S.C.Z.; investigation, G.M., F.D., L.F.L., M.L.T., M.L.F., S.T., and S.C.Z.; resources, F.D., L.F.L., G.M., M.L.F., and A.S.A.; writing—Original draft preparation, F.D. and M.L.T.; writing—Review and editing, F.D., G.M., L.F.L., M.L.T., and M.L.F.; visualization, F.D., L.F.L., and M.L.T.; supervision, F.D., L.F.L., M.L.F., and A.S.A.; project administration, F.D., M.L.F., and A.S.A.; funding acquisition, F.D., L.F.L., and G.M. All authors have read and agreed to the published version of the manuscript.

Funding: “This research was funded by PON02_00153_2939517—Tecnologie ed alta efficienza per la sostenibilità energetica ed ambientale on-board (TESEO).” The APC was funded by Francesca Deganello, Giuliana Magnacca and Leonarda Francesca Liotta”.

Acknowledgments: PON02_00153_2939517—tecnologie ed alta efficienza per la sostenibilità energetica ed ambientale on-board (TESEO) is greatly acknowledged. The authors are grateful to the CNR-ISMN Palermo technician Francesco Giordano for XRD measurements. GIA (Grant In Aid) 2018–2019 (I cycle) from ICDD (Grantee: Chiara Aliotta, grant ID: 18-01; editorial number: I08994; Sr_{0.85}Ce_{0.15}Fe_{0.67}Co_{0.33}O₃) is also acknowledged.

Conflicts of Interest: The authors declare no conflict of interest. The funders had no role in the design of the study; in the collection, analyses, or interpretation of data; in the writing of the manuscript, or in the decision to publish the results.

References

1. Varma, A.; Mukasyan, A.S.; Rogachev, A.S.; Manukyan, K.V. Solution Combustion Synthesis of Nanoscale Materials. *Chem. Rev.* **2016**, *116*, 14493–14586. [[CrossRef](#)]
2. Deganello, F.; Tyagi, A.K. Solution combustion synthesis, energy and environment: Best parameters for better materials. *Prog. Cryst. Growth Charact. Mater.* **2018**, *64*, 23–61. [[CrossRef](#)]

3. Deganello, F.; Testa, M.L.; La Parola, V.; Longo, A.; Tavares, A.C. LaFeO₃-based nanopowders prepared by a soft-hard templating approach: The effect of silica texture. *J. Mater. Chem. A* **2014**, *2*, 8438–8447. [[CrossRef](#)]
4. Thoda, O.; Xanthopoulou, G.; Vekinis, G.; Chroneos, A. Review of Recent Studies on Solution Combustion Synthesis of Nanostructured Catalysts. *Adv. Eng. Mater.* **2018**, *20*, 1–30. [[CrossRef](#)]
5. Deganello, F. Nanomaterials for environmental and energy applications prepared by solution combustion based-methodologies: Role of the fuel. *Mater. Today Proc.* **2017**, *4*, 5507–5516. [[CrossRef](#)]
6. Podbolotov, K.B.; Khort, A.A.; Tarasov, A.B.; Trusov, G.V.; Roslyakov, S.I.; Mukasyan, A.S. Solution Combustion Synthesis of Copper Nanopowders: The Fuel Effect. *Combust. Sci. Technol.* **2017**, *189*, 1878–1890. [[CrossRef](#)]
7. Aliotta, C.; Liotta, L.F.; La Parola, V.; Martorana, A.; Muccillo, E.N.S.; Muccillo, R.; Deganello, F. Ceria-based electrolytes prepared by solution combustion synthesis: The role of fuel on the materials properties. *Appl. Catal. B Environ.* **2016**, *197*, 14–22. [[CrossRef](#)]
8. Amarilla, J.M.; Rojas, R.M.; Rojo, J.M. Understanding the sucrose-assisted combustion method: Effects of the atmosphere and fuel amount on the synthesis and electrochemical performances of LiNi_{0.5}Mn_{1.5}O₄ spinel. *J. Power Sources* **2011**, *196*, 5951–5959. [[CrossRef](#)]
9. Lakshmi, R.; Velmurugan, V.; Sasikumar, S. Preparation and Phase Evolution of Wollastonite by Sol-Gel Combustion Method Using Sucrose as the Fuel. *Combust. Sci. Technol.* **2013**, *185*, 1777–1785. [[CrossRef](#)]
10. Wang, B.; Zeng, L.; Huang, W.; Melkonyan, F.S.; Sheets, W.C.; Chi, L.; Bedzyk, M.J.; Marks, T.J.; Facchetti, A. Carbohydrate-Assisted Combustion Synthesis to Realize High-Performance Oxide Transistors. *J. Am. Chem. Soc.* **2016**, *138*, 7067–7074. [[CrossRef](#)]
11. Da Conceição, L.; Silva, A.M.; Ribeiro, N.F.P.; Souza, M.M.V.M. Combustion synthesis of La_{0.7}Sr_{0.3}Co_{0.5}Fe_{0.5}O₃ (LSCF) porous materials for application as cathode in IT-SOFC. *Mater. Res. Bull.* **2011**, *46*, 308–314. [[CrossRef](#)]
12. Sihaib, Z.; Puleo, F.; Pantaleo, G.; La Parola, V.; Valverde, J.L.; Gil, S.; Liotta, L.F.; Fendler, A.G. The effect of citric acid concentration on the properties of LaMnO₃ as a catalyst for hydrocarbon oxidation. *Catalysts* **2019**, *9*, 226. [[CrossRef](#)]
13. Gabal, M.A.; Al-Juaid, A.A.; El-Rashed, S.; Hussein, M.A. Synthesis and characterization of nano-sized CoFe₂O₄ via facile methods: A comparative study. *Mater. Res. Bull.* **2017**, *89*, 68–78. [[CrossRef](#)]
14. Mohan, E.H.; Siddhartha, V.; Gopalan, R.; Rao, T.N.; Rangappa, D. Urea and sucrose assisted combustion synthesis of LiFePO₄/C nano-powder for lithium-ion battery cathode application. *AIMS Mater. Sci.* **2014**, *1*, 191–201. [[CrossRef](#)]
15. Li, S.; Bergman, B.; Zhao, Z. Synthesis and characterization of lanthanum aluminate powders via a polymer complexing plus combustion route. *Mater. Chem. Phys.* **2012**, *132*, 309–315. [[CrossRef](#)]
16. Chen, J.; Spear, S.K.; Huddleston, J.G.; Rogers, R.D. Polyethylene glycol and solutions of polyethylene glycol as green reaction media. *Green Chem.* **2005**, *7*, 64–82.
17. El Khalfaouy, R.; Addaou, A.; Laajeb, A.; Lahsini, A. Solution combustion synthesis of LiMnPO₄/C cathode material: The effect of four fuel sources on the electrochemical performances. *Int. J. Hydrogen Energy* **2019**, *44*, 18272–18282. [[CrossRef](#)]
18. Bu, S.; Jin, Z.; Liu, X.; Du, H.; Cheng, Z. Preparation and formation mechanism of porous TiO₂ films using PEG and alcohol solvent as double-templates. *J. Sol-Gel Sci. Technol.* **2004**, *30*, 239–248. [[CrossRef](#)]
19. Abdollahifar, M.; Huang, S.S.; Lin, Y.H.; Lin, Y.C.; Shih, B.Y.; Sheu, H.S.; Liao, Y.F.; Wu, N.L. High-performance carbon-coated ZnMn₂O₄ nanocrystallite supercapacitors with tailored microstructures enabled by a novel solution combustion method. *J. Power Sources* **2018**, *378*, 90–97. [[CrossRef](#)]
20. Zeng, M.; Fang, Z.; Xu, C. Novel method of preparing microporous membrane by selective dissolution of chitosan/polyethylene glycol blend membrane. *J. Appl. Polym. Sci.* **2004**, *91*, 2840–2847. [[CrossRef](#)]
21. Tarragó, D.P.; Malfatti, C.F.; de Sousa, V.C. Influence of fuel on morphology of LSM powders obtained by solution combustion synthesis. *Powder Technol.* **2015**, *269*, 481–487. [[CrossRef](#)]
22. Deganello, F.; Liotta, L.F.; Marci, G.; Fabbri, E.; Traversa, E. Strontium and iron-doped barium cobaltite prepared by solution combustion synthesis: Exploring a mixed-fuel approach for tailored intermediate temperature solid oxide fuel cell cathode materials. *Mater. Renew. Sustain. Energy* **2013**, *2*, 8. [[CrossRef](#)]
23. Kalantari Bolaghi, Z.; Hasheminasari, M.; Masoudpanah, S.M. Solution combustion synthesis of ZnO powders using mixture of fuels in closed system. *Ceram. Int.* **2018**, *44*, 12684–12690. [[CrossRef](#)]

24. Giuliano, A.; Carpanese, M.P.; Clematis, D.; Boaro, M.; Pappacena, A.; Deganello, F.; Liotta, L.F.; Barbucci, A. Infiltration, overpotential and ageing effects on cathodes for solid oxide fuel cells: $\text{La}_{0.6}\text{Sr}_{0.4}\text{Co}_{0.2}\text{Fe}_{0.8}\text{O}_{3-\delta}$ versus $\text{Ba}_{0.5}\text{Sr}_{0.5}\text{Co}_{0.8}\text{Fe}_{0.2}\text{O}_{3-\delta}$. *J. Electrochem. Soc.* **2017**, *164*, F3114–F3122. [[CrossRef](#)]
25. Kamata, K. Perovskite oxide catalysts for liquid-phase organic reactions. *Bull. Chem. Soc. Jpn.* **2019**, *92*, 133–151. [[CrossRef](#)]
26. Polo-Garzon, F.; Wu, Z. Acid-base catalysis over perovskites: A review. *J. Mater. Chem. A* **2018**, *6*, 2877–2894. [[CrossRef](#)]
27. Shin, H.H.; Mullins, C.B.; Goodenough, J.B. Oxygen-Electrode Catalysis on Oxoperovskites at 700 °C versus 20 °C. *Chem. Mater.* **2018**, *30*, 629–635. [[CrossRef](#)]
28. Li, C.; Soh, K.C.K.; Wu, P. Formability of ABO_3 perovskites. *J. Alloys Compd.* **2004**, *372*, 40–48. [[CrossRef](#)]
29. Sunarso, J.; Hashim, S.S.; Zhu, N.; Zhou, W. Perovskite oxides applications in high temperature oxygen separation, solid oxide fuel cell and membrane reactor: A review. *Prog. Energy Combust. Sci.* **2017**, *61*, 57–77. [[CrossRef](#)]
30. Brett, D.J.L.; Atkinson, A.; Brandon, N.P.; Skinner, S.J. Intermediate temperature solid oxide fuel cells. *Chem. Soc. Rev.* **2008**, *37*, 1568–1578. [[CrossRef](#)]
31. Abdalla, A.M.; Hossain, S.; Azad, A.T.; Petra, P.M.I.; Begum, F.; Eriksson, S.G.; Azad, A.K. Nanomaterials for solid oxide fuel cells: A review. *Renew. Sustain. Energy Rev.* **2018**, *82*, 353–368. [[CrossRef](#)]
32. Molenda, J.; Świerczek, K.; Zajac, W. Functional materials for the IT-SOFC. *J. Power Sources* **2007**, *173*, 657–670. [[CrossRef](#)]
33. Clematis, D.; Barbucci, A.; Presto, S.; Viviani, M.; Carpanese, M.P. Electrocatalytic activity of perovskite-based cathodes for solid oxide fuel cells. *Int. J. Hydrogen Energy* **2019**, *44*, 6212–6222. [[CrossRef](#)]
34. Lo Faro, M.; Aricò, A.S. Electrochemical behaviour of an all-perovskite-based intermediate temperature solid oxide fuel cell. *Int. J. Hydrogen Energy* **2013**, *38*, 14773–14778. [[CrossRef](#)]
35. Li, Z.; Li, S.; Tseng, C.J.; Tao, S.; Xie, K. Redox-reversible perovskite ferrite cathode for high temperature solid oxide steam electrolyser. *Electrochim. Acta* **2017**, *229*, 48–54. [[CrossRef](#)]
36. Su, C.; Wang, W.; Liu, M.; Tadé, M.O.; Shao, Z. Progress and Prospects in Symmetrical Solid Oxide Fuel Cells with Two Identical Electrodes. *Adv. Energy Mater.* **2015**, *5*, 1–19.
37. Dos Santos-Gómez, L.; Compana, J.M.; Bruque, S.; Losilla, E.R.; Marrero-López, D. Symmetric electrodes for solid oxide fuel cells based on Zr-doped $\text{SrFeO}_{3-\delta}$. *J. Power Sources* **2015**, *279*, 419–427. [[CrossRef](#)]
38. Jiang, S.P. Development of lanthanum strontium cobalt ferrite perovskite electrodes of solid oxide fuel cells—A review. *Int. J. Hydrogen Energy* **2019**, *44*, 7448–7493. [[CrossRef](#)]
39. Wang, Y.; Wang, Z.; Jin, C.; Li, C.; Li, X.; Li, Y.; Yang, R.; Liu, M. Enhanced overall water electrolysis on a bifunctional perovskite oxide through interfacial engineering. *Electrochim. Acta* **2019**, *318*, 120–129. [[CrossRef](#)]
40. Deganello, F.; Liotta, L.F.; Longo, A.; Casaletto, M.P.; Scopelliti, M. Cerium effect on the phase structure, phase stability and redox properties of Ce-doped strontium ferrates. *J. Solid State Chem.* **2006**, *179*, 3406–3419. [[CrossRef](#)]
41. Ikeda, H.; Nikata, S.; Hirakawa, E.; Tsuchida, A.; Miura, N. Oxygen sorption/desorption behavior and crystal structural change for $\text{SrFeO}_{3-\delta}$. *Chem. Eng. Sci.* **2016**, *147*, 166–172. [[CrossRef](#)]
42. Jiang, S.; Sunarso, J.; Zhou, W.; Shen, J.; Ran, R.; Shao, Z. Cobalt-free $\text{SrNbxFe}_{1-x}\text{O}_{3-\delta}$ ($x = 0.05, 0.1$ and 0.2) perovskite cathodes for intermediate temperature solid oxide fuel cells. *J. Power Sources* **2015**, *298*, 209–216. [[CrossRef](#)]
43. Fernández-Ropero, A.J.; Porras-Vázquez, J.M.; Cabeza, A.; Slater, P.R.; Marrero-López, D.; Losilla, E.R. High valence transition metal doped strontium ferrites for electrode materials in symmetrical SOFCs. *J. Power Sources* **2014**, *249*, 405–413. [[CrossRef](#)]
44. Deganello, F.; Liotta, L.F.; Leonardi, S.G.; Neri, G. Electrochemical properties of Ce-doped SrFeO_3 perovskites-modified electrodes towards hydrogen peroxide oxidation. *Electrochim. Acta* **2016**, *190*, 939–947. [[CrossRef](#)]
45. Tummino, M.L.; Laurenti, E.; Deganello, F.; Bianco Prevot, A.; Magnacca, G. Revisiting the catalytic activity of a doped SrFeO_3 for water pollutants removal: Effect of light and temperature. *Appl. Catal. B Environ.* **2017**, *207*, 174–181. [[CrossRef](#)]
46. Markov, A.A.; Nikitin, S.S.; Leonidov, I.A.; Patrakeev, M.V. Oxygen and electron transport in $\text{Ce}_{0.1}\text{Sr}_{0.9}\text{FeO}_{3-\delta}$. *Solid State Ion.* **2020**, *344*, 115131. [[CrossRef](#)]

47. Istomin, S.Y.; Antipov, E. V Cathode materials based on perovskite-like transition metal oxides for intermediate temperature solid oxide fuel cells. *Russ. Chem. Rev.* **2013**, *82*, 686–700. [[CrossRef](#)]
48. Choi, H.; Fuller, A.; Davis, J.; Wielgus, C.; Ozkan, U.S. Ce-doped strontium cobalt ferrite perovskites as cathode catalysts for solid oxide fuel cells: Effect of dopant concentration. *Appl. Catal. B Environ.* **2012**, *127*, 336–341. [[CrossRef](#)]
49. Wiik, K.; Aasland, S.; Hansen, H.; Tangen, I.; Ødegård, R. Oxygen permeation in the system $\text{SrFeO}_{3-x}\text{-SrCoO}_{3-y}$. *Solid State Ion.* **2002**, *152*, 675–680. [[CrossRef](#)]
50. Choi, H.; Fuller, A.; Dogu, D.; Binkley, K.E.; Davis, J.; Co, A.; Ozkan, U.S. Effect of Ce Doping on the Performance and Stability of Strontium Cobalt Ferrite Perovskites as SOFC Anode Catalysts. *Top. Catal.* **2015**, *58*, 359–374. [[CrossRef](#)]
51. Gwon, O.; Yoo, S.; Shin, J.; Kim, G. Optimization of $\text{La}_{1-x}\text{Sr}_x\text{CoO}_{3-\delta}$ perovskite cathodes for intermediate temperature solid oxide fuel cells through the analysis of crystal structure and electrical properties. *Int. J. Hydrogen Energy* **2014**, *39*, 20806–20811. [[CrossRef](#)]
52. Xu, X.; Pan, Y.; Zhou, W.; Chen, Y.; Zhang, Z.; Shao, Z. Toward Enhanced Oxygen Evolution on Perovskite Oxides Synthesized from Different Approaches: A Case Study of $\text{Ba}_{0.5}\text{Sr}_{0.5}\text{Co}_{0.8}\text{Fe}_{0.2}\text{O}_{3-\delta}$. *Electrochim. Acta* **2016**, *219*, 553–559. [[CrossRef](#)]
53. Li, S.; Hao, X.; Abudula, A.; Guan, G. Nanostructured Co-based bifunctional electrocatalysts for energy conversion and storage: Current status and perspectives. *J. Mater. Chem. A* **2019**, *7*, 18674–18707. [[CrossRef](#)]
54. Baharuddin, N.A.; Muchtar, A.; Somalu, M.R. Short review on cobalt-free cathodes for solid oxide fuel cells. *Int. J. Hydrogen Energy* **2017**, *42*, 9149–9155. [[CrossRef](#)]
55. Gao, L.; Zhu, M.; Li, Q.; Sun, L.; Zhao, H.; Grenier, J.C. Electrode properties of Cu-doped $\text{Bi}_{0.5}\text{Sr}_{0.5}\text{FeO}_{3-\delta}$ cobalt-free perovskite as cathode for intermediate-temperature solid oxide fuel cells. *J. Alloys Compd.* **2017**, *700*, 29–36. [[CrossRef](#)]
56. Trofimenko, N.E.; Ullmann, H. Oxygen stoichiometry and mixed ionic-electronic conductivity of $\text{Sr}_{1-a}\text{Ce}_a\text{Fe}_{1-b}\text{Co}_b\text{O}_{3-x}$ perovskite-type oxides. *J. Eur. Ceram. Soc.* **2000**, *20*, 1241–1250. [[CrossRef](#)]
57. Hansen, K.K. Evaluation of LSF based SOFC cathodes using cone-shaped electrodes and EIS. *Solid State Ion.* **2020**, *344*, 115096. [[CrossRef](#)]
58. Bogan, M.J.; Agnes, G.R. Poly (ethylene glycol) doubly and singly cationized by different alkali metal ions: Relative cation affinities and cation-dependent resolution in a quadrupole ion trap mass spectrometer. *J. Am. Soc. Mass Spectrom.* **2002**, *13*, 177–186. [[CrossRef](#)]
59. Nikolić, A.S.; Jović, N.; Rogan, J.; Kremenović, A.; Ristić, M.; Meden, A.; Antić, B. Carboxylic acids and polyethylene glycol assisted synthesis of nanocrystalline nickel ferrites. *Ceram. Int.* **2013**, *39*, 6681–6688. [[CrossRef](#)]
60. Yang, W.; Zhang, H.; Sun, C.; Liu, L.; Alonso, J.A.; Fernández-Díaz, M.T.; Chen, L. Insight into the structure and functional application of the $\text{Sr}_{0.95}\text{Ce}_{0.05}\text{CoO}_{3-\delta}$ cathode for solid oxide fuel cells. *Inorg. Chem.* **2015**, *54*, 3477–3484. [[CrossRef](#)]
61. Tiwari, S.; Balasubramanian, N.; Biring, S.; Sen, S. Synthesis, structure and characterization of Co doped CeO_2 nanoparticles. *IOP Conf. Ser. Mater. Sci. Eng.* **2018**, *396*, 012035. [[CrossRef](#)]
62. ahsanzadeh-Vadeqani, M.; Razavi, R.S.; Barekat, M.; Borhani, G.H.; Mishra, A.K. Preparation of yttria nanopowders for use in transparent ceramics by dry ball-milling technique. *J. Eur. Ceram. Soc.* **2017**, *37*, 2169–2177. [[CrossRef](#)]
63. Carvalho, M.D.; Ferreira, L.P.; Colomer, M.T.; Gaczyński, P.; Cruz, M.M.; Waerenborgh, J.C.; Godinho, M. Magnetic studies on $\text{Sr}_{0.8}\text{Ce}_{0.1}\text{Fe}_{0.7}\text{Co}_{0.3}\text{O}_{3-\delta}$ perovskite. *Solid State Sci.* **2006**, *8*, 444–449. [[CrossRef](#)]
64. Deganello, F.; Tummino, M.L.; Calabrese, C.; Testa, M.L.; Avetta, P.; Fabbri, D.; Prevot, A.B.; Montoneri, E.; Magnacca, G. A new, sustainable LaFeO_3 material prepared from biowaste-sourced soluble substances. *New J. Chem.* **2015**, *39*, 877–885. [[CrossRef](#)]
65. Magnacca, G.; Spezzati, G.; Deganello, F.; Testa, M.L. A new in situ methodology for the quantification of the oxygen storage potential in perovskite-type materials. *RSC Adv.* **2013**, *3*, 26352–26360. [[CrossRef](#)]
66. Royer, S.; Bérubé, F.; Kaliaguine, S. Effect of the synthesis conditions on the redox and catalytic properties in oxidation reactions of $\text{LaCo}_{1-x}\text{Fe}_x\text{O}_3$. *Appl. Catal. A Gen.* **2005**, *282*, 273–284. [[CrossRef](#)]
67. Lan, R.; Cowin, P.I.; Sengodan, S.; Tao, S. A perovskite oxide with high conductivities in both air and reducing atmosphere for use as electrode for solid oxide fuel cells. *Sci. Rep.* **2016**, *6*, 4–11. [[CrossRef](#)]

68. Ganopadhyay, S.; Masunov, A.E.; Inerbaev, T.; Mesit, J.; Guha, R.K.; Sleiti, A.K.; Kapat, J.S. Understanding oxygen vacancy migration and clustering in barium strontiumcobalt iron oxide. *Solid State Ion.* **2010**, *181*, 1067–1073. [[CrossRef](#)]
69. Toby, B.H. EXPGUI, a graphical user interface for GSAS. *J. Appl. Crystallogr.* **2001**, *24*, 210–213. [[CrossRef](#)]
70. Toby, B.H. R factors in Rietveld analysis: How good is good enough? *Powder Diffr.* **2006**, *21*, 67–70. [[CrossRef](#)]
71. Jansen, E.; Schaefer, W.; Will, G. R values in analysis of powder diffraction data using Rietveld refinement. *J. Appl. Crystallogr.* **1994**, *27*, 492–496. [[CrossRef](#)]
72. Brunauer, S.; Emmett, P.H.; Teller, E. Adsorption of Gases in Multimolecular Layers. *J. Am. Chem. Soc.* **1938**, *2*, 309–319. [[CrossRef](#)]
73. Barrett, E.P.; Joyner, L.G.; Halenda, P.P. The Determination of Pore Volume and Area Distributions in Porous Substances. I. Computations from Nitrogen Isotherms. *J. Am. Chem. Soc.* **1951**, *73*, 373–380. [[CrossRef](#)]
74. Dunyushkina, L.A.; Lu, Y.; Adler, S.B. Microelectrode array for isolation of electrode polarization on planar solid electrolytes. *J. Electrochem. Soc.* **2005**, *152*. [[CrossRef](#)]



© 2020 by the authors. Licensee MDPI, Basel, Switzerland. This article is an open access article distributed under the terms and conditions of the Creative Commons Attribution (CC BY) license (<http://creativecommons.org/licenses/by/4.0/>).